Research Article | Vol. 28, No. 18 / 31 August 2020 / Optics Express 27096
Optics EXPRESS

Visualization of ultrasonic wave field by stroboscopic polarization selective imaging

GAOSHANG LIU,[1,4] JICHUAN XIONG,[1,4] YUN CAO,[1] RUIJIE HOU,[1] LISHAN ZHI,[1] ZHIYING XIA,[1] WEIPING LIU,[1] XUEFENG LIU,[1,*] CHRIST GLORIEUX,[2] JOHN H. MARSH,[3] AND LIANPING HOU[3]

[1]*School of Electronic and Optical Engineering, Nanjing University of Science and Technology, Nanjing 210094, China*
[2]*Laboratory of Acoustics - Soft Matter and Biophysics, Department of Physics and Astronomy, KU Leuven, Celestijnenlaan 200D, 3001, Belgium*
[3]*James Watt School of Engineering, University of Glasgow, Glasgow G12 8QQ, UK*
[4]*These authors contributed equally to this work*
[*]*liuxf1956@163.com*

Abstract: A stroboscopic method based on polarization selective imaging is proposed for dynamic visualization of ultrasonic waves propagating in a transparent medium. Multiple independent polarization parametric images were obtained, which enabled quantitative evaluation of the distribution of the ultrasonic pressure in quartz. In addition to the detection of optical phase differences δ in conventional photo-elastic techniques, the azimuthal angle φ and the Stokes parameter S_2 of the polarized light are found to be highly sensitive to the wave-induced refraction index distribution, opening a new window on ultrasonic field visualization.

1. Introduction

Quantitative measurement of ultrasonic waves forms the basis of a wide variety of ultrasonic applications, such as defect inspection of components [1,2], medical ultrasound diagnostics [3,4], and photoacoustic tomography (PAT) of biomedical tissues [5]. Ultrasonic detectors with broad detection bandwidth, small size, high speed, high sensitivity and good spatial resolution, are desired for ultrasonic visualization in the above applications. Currently, contact ultrasonic detection is widely utilized due to its high sensitivity and commercial maturity. This concept typically makes use of ultrasonic transducers, e.g. piezoelectric sensors, to convert the sound wave pressure to electrical signals. These transducers are sensitive enough for most applications but are limited in their detection bandwidth and spatial resolution. There is therefore a growing interest in non-contact optical detection methods, with the goal of overcoming the above limitations. In these methods, visualization of ultrasonic waves is mainly achieved by measuring the effect of ultrasonically induced strain on an optical wave passing through or reflecting from the medium. Since ultrasonic strain goes along with a modified refractive index, the passage of an ultrasonic wave affects the polarization status, phase or frequency of the optical wave used for detection. The resulting variations in optical parameters can then be converted into variations in optical intensity by an interferometric or polarimetric detection scheme, and recorded by using a photodiode or optical imaging sensor. Hence, the evolution of an ultrasonic wave field can be inferred from a recorded intensity distribution.

Several optical techniques have been applied for vibrometric measurements in various transparent and non-transparent materials. Laser Doppler vibrometry (LDV) is an interferometric technique widely used for scanning measurements and two-dimensional reconstruction of the acoustic field by demodulating the frequency change of the optical wave at each detection point [6–10]. A so-called laser beam microphone method has been used to visualize the spatial distribution of the sound field in a scanning manner [11]. However, scanning measurements

#400355 https://doi.org/10.1364/OE.400355
Journal © 2020 Received 19 Jun 2020; revised 31 Jul 2020; accepted 18 Aug 2020; published 28 Aug 2020

Optics EXPRESS

can be quite time-consuming. In order to address this issue, full-field imaging methods based on diffraction and interferometry polarimetry have been developed to visualize variations of the detection optical wave induced by the acoustic waves [12,13]. By combining with a stroboscopic timing scheme, transient surface acoustic waves have been dynamically visualized with photorefractive interferometry [14] and white-light interferometry [15]. Also, Schlieren photography has been utilized to image the dynamic sound pressure in the air [16,17]. A sensitive optical interferometer based on diffractive optics has been reported to image thermoelastic strain of non-transparent materials quantitatively [18].

An improved photoelastic visualization system has been utilized to evaluate the ultrasonic wave field synthesized by a phased array ultrasonic system [19]. Acoustic evanescent waves have been successfully visualized by a stroboscopic photoelastic method with high spatial resolution [20]. The photoelastic method was also elaborated to quantitatively evaluate the acoustic waves by modulating two orthogonal polarizers [21,22]. But it was subject to a low imaging speed.

In current photoelastic techniques, the evaluation of ultrasonic waves is based on measurement of the phase retardation δ of polarized light. However, the azimuthal angle of the polarized light, ϕ, which is another optical wave parameter that carries information about the ultrasonic waves, is often neglected. Our group has proposed the parametric indirect microscopic imaging method (PIMI), which allows both the phase retardation and the ellipticity azimuthal angle to be measured simultaneously [23]. The method maps the variations of the polarization state induced by static stress with high resolution. This method has been extended for visualizing an ultrasound field [24]. Untill now, it has been limited in measurement speed and the interpretation of results has been hindered due to spurious interference patterns produced by multiple reflections from different parts of the sample. Furthermore, the required rotation of the polarizer during the measurement leads to mechanical vibrations of the optical system, which acts as a source of noise. Furthermore, because the sample was illuminated by a continuous laser, the temporal resolution of the system was determined by the electronic shutter of the camera.

Recently, polarization charge-coupled device (CCD) cameras have been developed, which allow images to be taken at different polarization directions in a single exposure [25–27]. Researchers have made use of such devices to image the dynamic birefringence induced by ultrasonic fields via the stress-optic effect up to high frame rates, i.e. 1.3 MHz and 1,550,000 fps, respectively [28,29]. The highest frequency of ultrasound that can be detected by such systems is determined by the shortest exposure time t_c of the camera. According to the Nyquist sampling theorem, the upper limit frequency of ultrasound that can be detected is $1/(2t_c)$. Although the measurement speed is relatively fast, these techniques are limited either by the pixel density of the images or the upper-frequency limit of measurable ultrasonic waves. Furthermore, extra information carried by other independent polarization parameters of the detection beam, e.g. the azimuthal angle of the polarized light, has not been exploited [28,29].

In this paper, we propose a stroboscopic polarization selective imaging method to visualize the phase retardance and azimuthal angle of the detection optical wave. We utilize the approach to evaluate the ultrasonic field distribution with fast speed and high-resolution. Compared with previous work of the authors' group [24], the upper frequency limit of measurable ultrasound by the system is significantly improved by using a nanosecond pulsed laser as a stroboscopic illumination source. The short pulse duration, i.e. 10 ns, overcomes the above mentioned limitations of the relatively long electronic shutter time of current polarization cameras and allows the propagation of ultrasound at frequencies up to approximately 50 MHz to be observed. Besides, by avoiding to use a rotating polarizer, the mechanical vibration noise is eliminated and the image contrast is improved further. The polarization camera (PHX050S Lucid, with a resolution of 2448×2048 pixels) ensures the possibility of full-field imaging of an ultrasound field with a much bigger pixel number and spatial resolution than previously reported measurements using a polarization CCD [28,29]. Furthermore, the birefringent phase retardance and the azimuthal

Optics EXPRESS

angle can be imaged in a single exposure, which provides two independent measurements of the ultrasonic field simultaneously.

2. Methods

When ultrasonic waves propagate through a medium, the shear waves produce stress anisotropy. The stress anisotropy can be evaluated by measuring changes in an optical probing beam passing through the medium, which is affected by ultrasound-induced photoelastic effects. Assuming light passing through a thin specimen made of optically isotropic material, the magnitude of the relative phase retardation in the [1 2] *xy* plane can be described in 2D by the *stress-optic* law [30]:

$$\Delta\delta_{xy12} = \frac{2\pi}{\lambda}\int_0^d C(\sigma_x - \sigma_y)dz, \tag{1}$$

where $\Delta\delta_{xy12}$ is the stress-induced retardation, d is the specimen thickness, λ is the optical wavelength. This phase retardation changes the polarization status of the transmitted light. $C = c_2 - c_1$ is the relative stress-optic coefficient, where c_1, c_2 are stresses optic coefficients along the x and y axes, respectively and σ_x, σ_y are principal stresses along the x and y axes, respectively.

A schematic diagram of the stroboscopic polarization selective imaging is presented in Fig. 1.

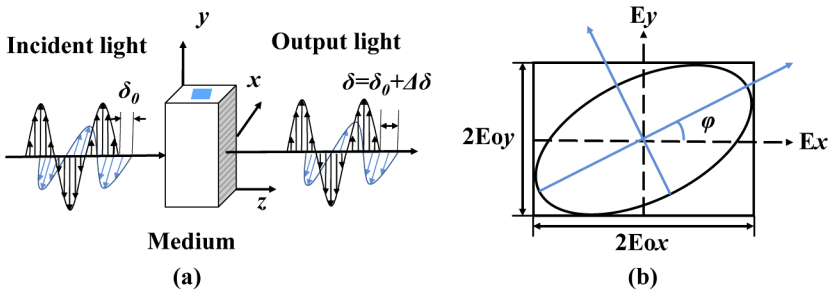

Fig. 1. Schematic diagram of the stroboscopic polarization selective imaging method. (a) Phase shift δ, (b) Azimuthal angle of polarized light φ.

When circularly polarized light passes through a transparent material exhibiting stress anisotropy, due to stress-induced effects, the orthogonal polarization components along the two principal stress directions experience different values of the refractive index. The phase retardation between the two orthogonal polarization components changes the polarization states of transmitted light. After passing through the specimen, the polarization states of the output light, as described by the polarization ellipse shown in Fig. 1(b), can be written as:

$$\frac{E_x^2}{E_{ox}^2} + \frac{E_y^2}{E_{oy}^2} - \frac{2E_xE_y}{E_{ox}E_{oy}}cos\delta = sin^2\delta, \tag{2}$$

where E_x and E_y are the electric vector components of the output light, E_{ox} and E_{oy} are the amplitudes of the output light, along the x and y axes, respectively.

The Stokes polarization parameters of the polarized light can be calculated through the four different polarization directional images [31]:

$$\begin{cases} S_0 = E_{ox}^2 + E_{oy}^2 = I(0°) + I(90°) \\ S_1 = E_{ox}^2 - E_{oy}^2 = I(0°) - I(90°) \\ S_2 = 2E_{ox}E_{oy}cos\delta = I(45°) - I(135°) \\ S_3 = 2E_{ox}E_{oy}sin\delta = I_{RCP} - I_{LCP} \end{cases}, \tag{3}$$

Optics EXPRESS

where four polarized plates with different angles (0°, 45°, 90°, 135°) are used to detect the polarized light. $I(0°)$ is the intensity of linearly horizontal polarized light component, $I(90°)$ is the intensity of linearly vertical polarized light component, $I(45°)$ is the intensity of linear +45° polarized (L+45P) light component, $I(135°)$ is the intensity of linear -45° polarized (L-45P) light components, I_{RCP} is the intensity of the right circularly polarized light component, I_{LCP} is the intensity of the left circularly polarized light component. The quantities S_0, S_1, S_2 and S_3 are the observables of the output polarized field. The first Stokes parameter S_0 describes the total intensity of the optical beam; the second parameter S_1 describes the preponderance of linearly horizontal polarized (LHP) light over linearly vertical polarized (LVP) light; the third parameter S_2 describes preponderance of L+45P light over L-45P light and, finally, S_3 describes the preponderance of right circularly polarized (RCP) light over left circularly polarized (LCP) light.

Given the above definitions, the phase difference δ can be written in terms of the Stokes parameter:

$$\delta = \arccos\left(\frac{S_2}{2\sqrt{I(0^o)I(90^o)}}\right) = \arccos\left(\frac{I(45°) - I(135°)}{2\sqrt{I(0^o)I(90^o)}}\right), \tag{4}$$

The azimuthal angle φ of the polarized light can be written as follows:

$$\varphi = \frac{1}{2}tan^{-1}\left(\frac{S_2}{S_1}\right) = \frac{1}{2}tan^{-1}\left(\frac{I(45°) - I(135°)}{I(0°) - I(90°)}\right), \ -\frac{\pi}{4}<\varphi<\frac{\pi}{4} \tag{5}$$

By taking the pixels with polarization azimuth at 0°, 45°,90° and 135°, E_{ox}, E_{oy} and δ can be calculated using Eq. (3) and Eq. (4). The azimuthal angle φ can then be obtained from Eq. (5) and the stress distribution induced by the ultrasonic field can be reconstructed using Eq. (1).

3. Experimental setup

As illustrated in Fig. 2, the experimental setup consists of two parts: an optical imaging system and a synchronization controlling system. The optical part of the system includes a pulsed frequency-doubled Nd:YAG laser, a beam expander (BE), a polarizer (P), a quarter-wave plate (QWP), a 4F imaging system (L1 and L2) and a polarization CCD. A pulsed Nd:YAG laser (Grace Laser TINY-200L, wavelength 532 nm, beam diameter ~5 mm) was used as the stroboscopic light source, providing an exposure time of about 10 ns. The linearly polarized beam from the laser was first expanded to about 10 mm by the beam expander. After passing through a polarizer and a quarter-wave plate with its fast axis oriented at 45° with respect to the transmission axis of the polarizer, the incident light was converted to circularly polarized light. Next, the collimated beam was passed through a transparent isotropic quartz glass with an ultrasonic wave transmitted from one end to the other transverse to the optical axis. As shown in Fig. 2(b), the ultrasonic wave was generated by a piezoelectric ceramic transducer (PZT 1) attached to the end face of the quartz glass, with size of 10 mm×10 mm×20 mm and 5 mm×7 mm for the glass and PZT, respectively. The polarization CCD (PHX050S Lucid, with a pixel size of 3.45 μm) acquired images of the sample through the 4F system and $I(0°)$, $I(90°)$, $I(45°)$, $I(135°)$ linear polarizers in a single exposure. In the experiment, transducer PZT 1, with a resonant frequency of 5 MHz, was used for generating the ultrasonic waves, which were monitored by PZT 2 at the opposite face of the sample.

A diagram for the timing of the stroboscopic exposure system is presented in Fig. 3(a), which collected images at different moments during the propagation of the ultrasonic wave from PZT 1 to PZT 2. Synchronization signals were used to trigger the generation of the ultrasonic wave, the laser illumination and the exposure of the imaging system. A trapezoidal pulse with a duration of 170 ns that was used to drive PZT 1 and a typical ultrasonic pressure signal captured by PZT 2 are shown in Figs. 3(b) and (c) respectively. The frame rate of the CCD camera is 10 fps. The

Optics EXPRESS

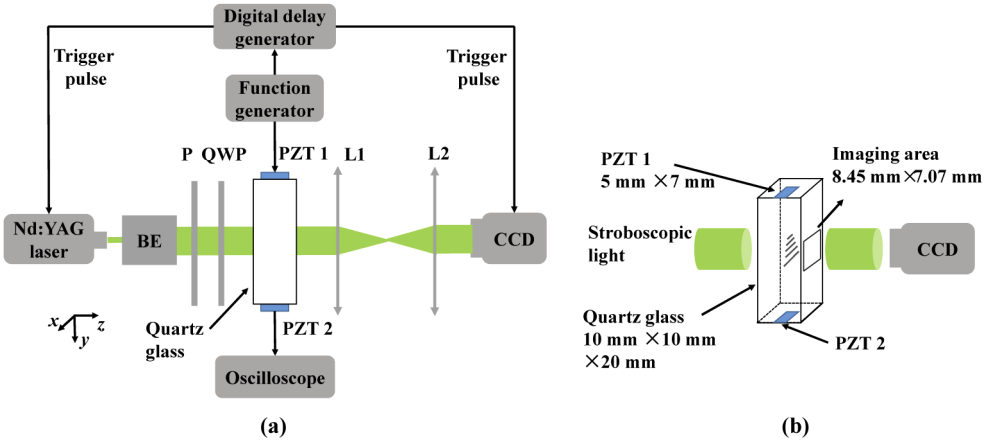

Fig. 2. Experimental setup for the stroboscopic polarization selective imaging of the ultrasonic field. (a) The stroboscopic light passes through a transparent isotropic quartz glass with ultrasonic wave transmitting from one end to the other. Two synchronization signals are used to trigger the generation of the ultrasonic wave and the exposure time of the imaging system. (b) The structure of sample.

repetition frequency of the laser pulse and the ultrasound excitation signal was 10 Hz and 5 kHz, respectively, as shown in Fig. 3(a). The excitation time of the PZT was delayed by 1 μs with respect to the output triggering signal of the laser, i.e. Q in Fig. 3(a). This delay is calculated as the time needed for the ultrasound propagating from the PZT to the area covered by the probe beam. The shutter of the camera was triggered to open before the output of the probe laser pulse and close after imaging the pulse. The delay between generation of the ultrasonic wave and the exposure period was set to ensure images taken when the ultrasonic wave-front was within the imaging area (approximately 8.45 mm × 7.07 mm) covered by the probe beam.

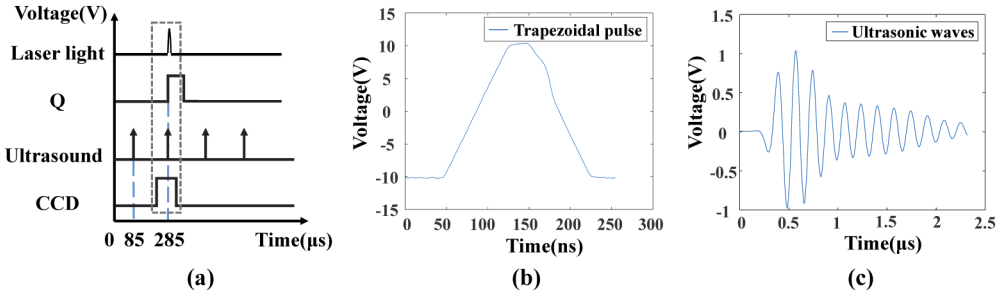

Fig. 3. (a) Timing chart of the stroboscopic system. (a) Q depicts the timing of the laser pulses. Trigger signals with a proper delay with respect to the ultrasonic generation pulse are used to trigger the polarization CCD and the pulsed laser, making the opening period of the CCD shutter covers the pulses from the laser. (b) A trapezoidal pulse with a duration of 170 ns is used to trigger PZT 1. (c) A typical ultrasonic pressure signal measured by PZT 2.

The utilization of a short pulse stroboscopic light source overcomes the limitation of the slow electronic shutter of the CCD and enables the system to visualize the ultrasonic wave dynamically with high temporal resolution.

Optics EXPRESS

4. Results and discussions

Figure 4 shows images of Stokes parameters, i.e. S_0 to S_3, phase retardation δ, and azimuthal angle φ, calculated from the $I(0°)$, $I(90°)$, $I(45°)$, $I(135°)$ linear polarized images acquired by the polarization CCD. The S_0 image in Fig. 4(a) represents the total intensity of light. The S_1 image in Fig. 4(b) is the difference between $I(0°)$ and $I(90°)$, and shows the output light is no longer circularly polarized after passing through the ultrasonic field. The S_2 image in Fig. 4(c), i.e. the difference between $I(45°)$ and $I(135°)$, shows the image includes information of the ultrasound field, but with relatively low contrast. As shown in Figs. 4(e) and (f), the images of the phase difference δ and the azimuthal angle φ demonstrate relatively high sensitivity to the ultrasonic field. The changes in the parameter δ are related to the sound-induced stress according to Eq. (1) and (4). Similarly, azimuthal angle ϕ is related to the stress distribution according to Eq. (5). These images represent the distribution of tangential displacement caused by the ultrasonic wave passing through the imaging area of the sample covered by the probe beam. The images (c), (e), (f) indicate the up-down symmetry, while the others indicate circular symmetry induced by the high coherence of the laser.

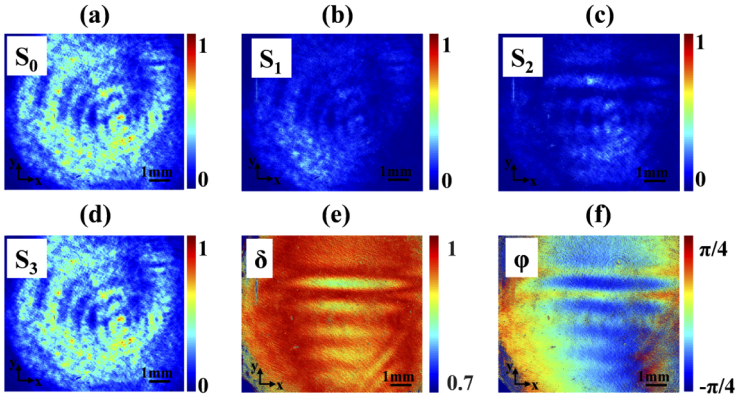

Fig. 4. Polarization parameters images. (a)-(d) Stokes parameters, respectively S_0, S_1, S_2, S_3. (e) Phase difference δ, (f) Azimuthal angle φ.

In order to analyse the sensitivities of different parametric polarization images, intensity profile curves were extracted from images of the parameter S_2, the phase difference δ, and the azimuthal angle φ, along the vertical line shown in Fig. 5. Figures 5(a) and (d) show the variation of δ is approximately identical to the measured ultrasonic pressure in Fig. 3(c). Figures 5(b) and (e) show parameter φ is even more sensitive, with a higher contrast and sensitivity to the ultrasonic pressure than δ. Besides, the intensity profile curve in Fig. 5(e) is similar but not identical to Fig. 3(c). This demonstrates that parameter S_2, i.e. Figures 5(c) and (f), is equivalent to the image that would be obtained in conventional photoelastic measurements.

Figure 6 shows time-sequential images of the ultrasonic wave propagation with a delay time step of 0.2 μs between subsequent images. In addition to the clear evolution of the main propagating ultrasonic wave, a reflected wave is also visible in the bottom right corner. The number of pixels corresponding to the distance propagated in one delay step is counted as 326, so with a pixel size of 3.45 μm, the actual distance is 326×3.45 μm $= 1124.7$ μm. The speed of the ultrasound propagating in quartz glass can then be calculated from the propagation distance and propagation time, i.e. approximately 5623.5 m/s, which is in accordance with literature values, ranging from 5570 m/s to 5930 m/s [32], validating the accuracy of the measurement system. Factors of uncertainty in this measurement include the relative delay error between triggering

Optics EXPRESS

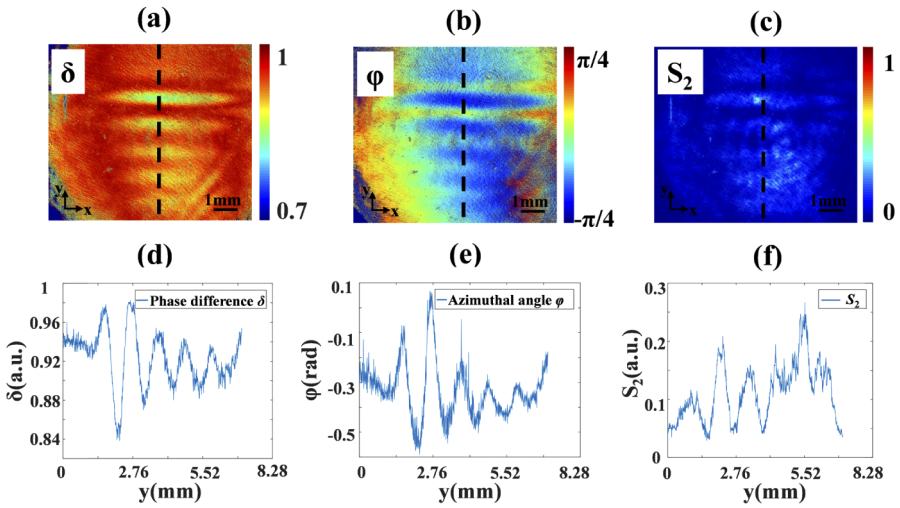

Fig. 5. Intensity profile curves of parametric polarization images. Intensity curves for (d) δ, (e) φ, and (f) S_2, extracted from (a) δ, (b) φ, (c) S_2 along the vertical dashed line respectively.

pulses from the function generator or the digital delay generator and the jitter time of the pulsed laser.

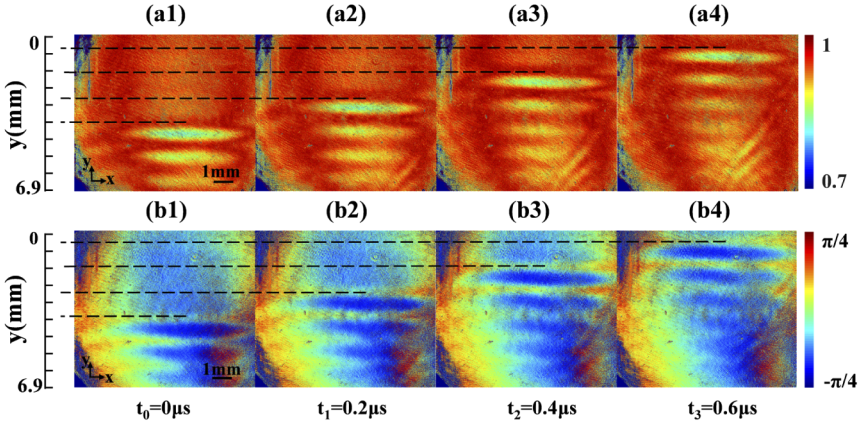

Fig. 6. Time-sequential images of the ultrasonic wave propagation with a delay step of 0.2μs between the subsequent stroboscopic illuminations. (a1) - -(a4) phase retardance δ images. (b1)- -(b4) the azimuthal angle φ images. No averaging was taken.

In order to analyse the frequency response of the system, a continuous sinusoidal input signal around the resonant frequency was applied to PZT 1. The experimental results are shown in Fig. 7. The polarization parametric images of δ and φ show the distribution of the ultrasonic induced stress under the same experimental conditions, except for a different frequency applied to PZT 1, i.e. 5 MHz to 6.5 MHz in steps of 0.1 MHz. The results illustrate that the imaging system has a relatively flat frequency response, which is important for detecting ultrasound with broad bandwidth. The frequency range of 5 MHz to 6.5 MHz was selected around the center frequency of the PZT in order to ensure the generated ultrasound had a flat amplitude across the frequency range.

Optics EXPRESS

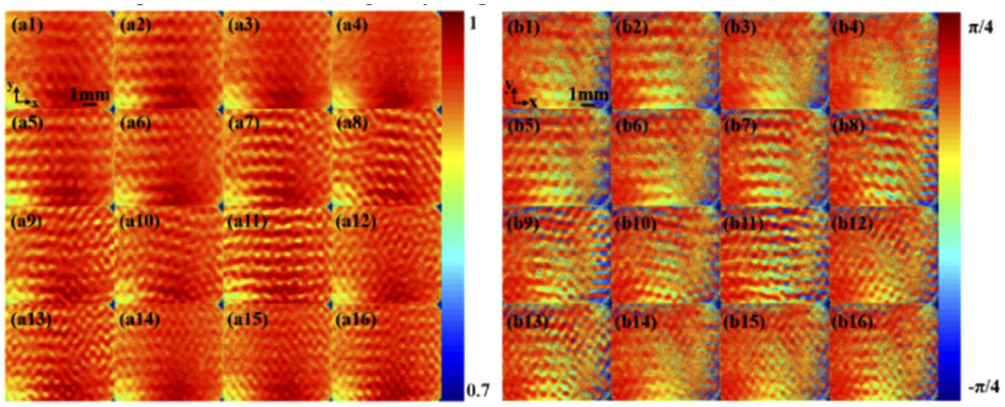

Fig. 7. Imaging results of ultrasound fields with different frequencies. The frequency ranged from 5 MHz to 6.5 MHz with 0.1 MHz step in (1)-(16), respectively. (a1)-(a16) are phase retardance δ images, (b1) -(b16) are azimuthal angle φ images.

As can be seen from Eq. (1), the phase retardation $\Delta\delta_{xy12}$ is directly proportional to the distribution of the ultrasonically induced stress. In other words, the phase retardation of the output light is proportional to the sound pressure. In order to illustrate the accuracy of this technique, numerical simulations were performed using the k-wave MATLAB toolbox [33] and compared with the experimental results. The simulation was configured with the same parameters of the experimental setup as described in section 3, including the sample size, transducer excitation signal, probe beam parameters, etc. The simulation was performed with a grid size of 46.3 µm × 46.3 µm, a time step of 2.46 ns, the sound speed of 5640 m/s, the attenuation coefficient of 0.75, and the initial sound pressure at the source PZT was configured to be the same as that of the pulse shown in Fig. 3(b). A comparison between the simulated sound pressure distribution and the experimental result of δ is shown in Fig. 8. Figures 8(a) and (b) show consistency in the distribution of ultrasound except for random noise in the image of δ. As shown in Fig. 8(c), the experimental measurements of the phase difference δ agree well with the simulated ultrasonic pressure distribution.

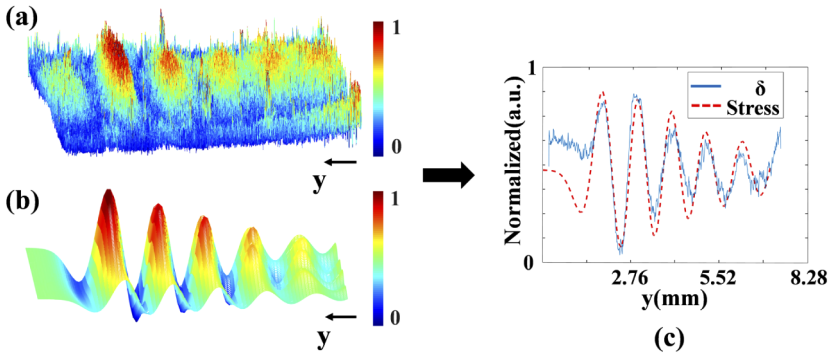

Fig. 8. Comparisons of experimental and simulated results. (a) A 3-dimensional image of δ, (b) 3-dimensional simulated image of ultrasound pressure, (c) intensity curves extracted from (a) and (b) along the y-axis.

Optics EXPRESS

5. Conclusion

In this article, an optical method for sensing and visualizing the ultrasonic wave using multiple polarization parameters of the probe light was implemented. A theoretical model for the quantitative relation between the ultrasonic wave field and the polarization parameters of the probe light has been elaborated. By utilizing a stroboscopic illumination method, parametric images of the phase difference δ, the azimuthal angle φ, and the Stokes parameters of the probe light were extracted from polarization images taken by a polarization CCD. It turns out that parametric images of δ, φ and Stokes S_2 are sensitive to the ultrasonic field, while S_0, S_1, S_3. are not or only weakly. Good agreement was found between snapshots of simulated ultrasonic pressure fields and parametric images of δ.

The results show that the proposed method can be used to visualize an ultrasonic field using multiple independent polarization parametric images, and that, provided the photoelastic coefficient, the effective optical path length, and the illumination condition of the sample are calibrated carafully, the ultrasonic pressure distribution can be evaluated quantitatively. This makes the technique very useful for fast and non-contact detection of ultrasonic waves in photoacoustic sensing and imaging applications when it is implemented in a reflection mode. However, extension of this method to image ultrasound wave propagation in turbid medium is facing various challenges such as the optical and acoustic scattering, low reflectivity, etc.

In future implementations, we will replace the Nd:YAG laser with a polarization controllable semiconductor laser source [34]. This will enable the measurement system to be miniaturized, the laser pulse frequency to be increased, and the polarization state of the light to be tuned rapidly [35]. In this way, it will be possible to average a large number of camera snapshots to increase the imaging quality. Furthermore, polarization-sensitive imaging can be achieved without an expensive polarization CCD, by controlling the polarization of the probe beam. To ensure sufficient light is available, a bar of such sources will be used, containing a number of semiconductor lasers operating incoherently. Multiple ridge waveguide semiconductor lasers each operating in a single transverse mode will be driven in parallel. In addition, low-current polarization controllers (one for each laser) will be driven in parallel to control the polarization state. This device will make it possible to generate optical pulses and rotate the polarization of the output on a timescale down to 10s of nanoseconds.

Funding

National Key Research and Development Program of China (2017YFF0107100); National Key Scientific Instrument and Equipment Development Projects of China (61827814); Natural Science Foundation of Beijing Municipality (Z190018); National Natural Science Foundation of China (51805268); Fundamental Research Funds for the Central Universities (30920010011); Ministry of Education Collaborative Project, "NDTonAIR" project (H2020-MSCA-ITN-2016- Grant 722134).

Disclosures

The authors declare no conflicts of interest.

References

1. K. Sun, L. Yuan, Z. Shen, Z. Xu, Q. Zhu, X. Ni, and J. Lu, "Scanning laser-line source technique for nondestructive evaluation of cracks in human teeth," Appl. Opt. **53**(11), 2366–2374 (2014).
2. Y. Ju, H. Xie, X. Zhao, L. Mao, Z. Ren, J. Zheng, F. Chiang, Y. Wang, and F. Gao, "Visualization method for stress-field evolution during rapid crack propagation using 3D printing and photoelastic testing techniques," Sci. Rep. **8**(1), 1–10 (2018).
3. K. Xia, X. Zhai, Z. Xie, K. Zhou, Y. Feng, G. Zhang, and C. Li, "Dual-modal photoacoustic/CT imaging system," Chin. Opt. Lett. **16**(12), 121701 (2018).

Optics EXPRESS

4. X. Zhu, Z. Huang, G. Wang, W. Li, D. Zou, and C. Li, "Ultrasonic detection based on polarization-dependent optical reflection," Opt. Lett. **42**(3), 439–441 (2017).
5. J. Xia, J. Yao, and L. V. Wang, "Photoacoustic tomography: principles and advances," Prog. Electromagn. Res. **147**, 1–22 (2014).
6. A. R. Harland, J. N. Petzing, and J. R. Tyrer, "Non-invasive measurements of underwater pressure fields using laser Doppler velocimetry," J. Sound Vib. **252**(1), 169–177 (2002).
7. L. Zipser, H. Franke, E. Olsson, N. E. Molin, and M. Sjödahl, "Reconstructing two-dimensional acoustic object fields by use of digital phase conjugation of scanning laser vibrometry recordings," Appl. Opt. **42**(29), 5831–5838 (2003).
8. A. Torras-Rosell, S. Barrera-Figueroa, and F. Jacobsen, "Sound field reconstruction using acousto-optic tomography," J. Acoust. Soc. Am. **131**(5), 3786–3793 (2012).
9. R. Malkin, T. Todd, and D. Robert, "A simple method for quantitative imaging of 2D acoustic fields using refracto-vibrometry," J. Sound Vib. **333**(19), 4473–4482 (2014).
10. K. Bertling, J. Perchoux, T. Taimre, R. Malkin, D. Robert, A.D. Rakíc, and T. Bosch, "Imaging of acoustic fields using optical feedback interferometry," Opt. Express **22**(24), 30346–30356 (2014).
11. T. Sakoda and Y. Sonoda, "Visualization of sound field with uniform phase distribution using laser beam microphone coupled with computerized tomography method," Acoust. Sci. & Tech. **29**(4), 295–299 (2008).
12. R. Miao, Z. Yang, J. Zhu, and C. Shen, "Visualization of low-frequency liquid surface acoustic waves by means of optical diffraction," Appl. Phys. Lett. **80**(17), 3033–3035 (2002).
13. T. Kakue, R. Yonesaka, T. Tahara, Y. Awatsuji, K. Nishio, S. Ura, T. Kubota, and O. Matoba, "High-speed phase imaging by parallel phase-shifting digital holography," Opt. Lett. **36**(21), 4131–4133 (2011).
14. J. Xiong, X. Xu, C. Glorieux, O. Matsuda, and L. Cheng, "Imaging of transient surface acoustic waves by full-field photorefractive interferometry," Rev. Sci. Instrum. **86**(5), 053107 (2015).
15. K. Kokkonen, L. Lipiäinen, I. Shavrin, S. Novotny, M. Kaivola, and H. Ludvigsen, "Characterization of surface acoustic waves by stroboscopic white-light interferometry," Opt. Express **23**(8), 9690–9695 (2015).
16. M. J. Hargather, G. S. Settles, and M. J. Madalis, "Schlieren imaging of loud sounds and weak shock waves in air near the limit of visibility," Shock Waves **20**(1), 9–17 (2010).
17. N. Chitanont, K. Yaginuma, K. Yatabe, and Y. Oikawa, "Visualization of sound field by means of Schlieren method with spatio-temporal filtering," in *proceedings of IEEE International Conference on Acoustics, Speech and Signal Processing* (IEEE 2015), pp. 509–513.
18. C. Glorieux, J. D. Beers, E. H. Bentefour, K. Van de Rostyne, and K. A. Nelson, "Phase mask based interferometer: Operation principle, performance, and application to thermoelastic phenomena," Rev. Sci. Instrum. **75**(9), 2906–2920 (2004).
19. S. Washimori, T. Mihara, and H. Tashiro, "Investigation of the sound field of phased array using the photoelastic visualization technique and the accurate FEM," Mater. Trans. **53**(4), 631–635 (2012).
20. K. Yamamoto, T. Sakiyama, and H. Izumiya, "Visualization of acoustic evanescent waves by the stroboscopic photoelastic method," Phys. Procedia **70**, 716–720 (2015).
21. Y. H. Nam and S. S. Lee, "A quantitative evaluation of elastic wave in solid by stroboscopic photoelasticity," J. Sound Vib. **259**(5), 1199–1207 (2003).
22. K. Date and Y. Udagawa, "Visualization of ultrasonic waves in a solid by stroboscopic photoelasticity and image processing techniques," in Review of Progress in Quantitative Nondestructive Evaluation (Springer, Boston, MA, 1989), pp. 1755–1762.
23. X. Liu, B. Qiu, Q. Chen, Z. Ni, Y. Jiang, M. Long, and L. Gui, "Characterization of graphene layers using super resolution polarization parameter indirect microscopic imaging," Opt. Express **22**(17), 20446–20456 (2014).
24. Y. Cao, J. Xiong, X. Liu, Z. Xia, W. Wang, N. P. Yadav, and W. Liu, "Sensing of ultrasonic fields based on polarization parametric indirect microscopic imaging," Chin. Opt. Lett. **17**(4), 041702 (2019).
25. V. Gruev, R. Perkins, and T. York, "CCD polarization imaging sensor with aluminum nanowire optical filters," Opt. Express **18**(18), 19087–19094 (2010).
26. N. Brock, B. Kimbrough T, and J. E. Millerd, "A pixelated micropolarizer-based camera for instantaneous interferometric measurements," *Proc. SPIE* 8160, 81600W (2011).
27. T. Ohfuchi, M. Sakakura, Y. Yamada, N. Fukuda, T. Takiya, Y. Shimotsuma, and K. Miura, "Polarization imaging camera with a waveplate array fabricated with a femtosecond laser inside silica glass," Opt. Express **25**(20), 23738–23754 (2017).
28. T. Onuma and Y. Otani, "A development of two-dimensional birefringence distribution measurement system with a sampling rate of 1.3 MHz," Opt. Commun. **315**, 69–73 (2014).
29. K. Ishikawa, K. Yatabe, N. Chitanont, Y. Ikeda, Y. Oikawa, T. Onuma, H. Niwa, and M. Yoshii, "High-speed imaging of sound using parallel phase-shifting interferometry," Opt. Express **24**(12), 12922–12932 (2016).
30. J. F. Doyle, J. W. Phillips, and D. Post, "Manual on Experimental Stress Analysis. Society for Experimental Mechanics," (1989).
31. E. Collett, "Field guide to polarization," in *SPIE Field Guides*, J. E. Greivenkamp, ed. (SPIE Press, 2005).
32. V. Deutsch, M. Platte, and M. Vogt, *Ultraschallprüfung: Grundlagen und industrielle Anwendungen* (Springer-Verlag, 2013).
33. B. E. Treeby, J. Jaros, D. Rohrbach, and B. T. Cox, "Modelling elastic wave propagation using the k-wave matlab toolbox," in *proceedings of 2014 IEEE international ultrasonics symposium* (IEEE, 2014), pp. 146–149.

Optics EXPRESS

34. B. M. Holmes, M. A. Naeem, D. C. Hutchings, J. H. Marsh, and A. E. Kelly, "A semiconductor laser with monolithically integrated dynamic polarization control," Opt. Express **20**(18), 20545–20550 (2012).
35. M. A. Naeem, M. Haji, B. M. Holmes, D. C. Hutchings, J. H. Marsh, and A E. Kelly, "Generation of high speed polarization modulated data using a monolithically integrated device," IEEE J. Sel. Top. Quantum Electron. **21**(4), 207–211 (2015).